Fracture flow simulation using a finite-difference lattice Boltzmann method

I. Kim* and W. B. Lindquist†
Department of Applied Mathematics and Statistics, Stony Brook University, Stony Brook, New York 11794-3600

W. B. Durham‡
Lawrence Livermore National Laboratory, Livermore, California 94550-9234

(Received 6 November 2002; published 24 April 2003)

We present numerical computations for single phase flow through three-dimensional digitized rock fractures under varied simulated confining pressures appropriate to midcrustal depths. The computations are performed using a finite difference, lattice Boltzmann method and thus simulate Navier-Stokes flow. The digitized fracture data sets come from profiled elevations taken on tensile induced fractures in Harcourt granite. Numerical predictions of fracture permeability are compared with laboratory measurements performed on the same fractures. Use of the finite difference lattice Boltzmann method allows computation on nonuniform grid spacing, enabling accurate resolution across the aperture width without extensive refinement in the other two directions.

DOI: 10.1103/PhysRevE.67.046708 PACS number(s): 02.70.Bf, 47.55.Mh, 46.50.+a, 47.11.+j

I. INTRODUCTION

Fluid flow in fractured rock is a subject of primary importance in petroleum engineering and hydrogeology. In the simplest approximation, single phase fluid flow through a fracture can be described by Poiseuille flow between smooth, parallel plates of separation (aperture width) h. In the parallel plate model fluid flow obeys Darcy's law [1],

$$Q=\frac{Ak}{\mu}\nabla P. \tag{1}$$

Our notation is standard: Q is the volumetric flow rate, the outlet flow area is $A=L_y h$, μ is the fluid viscosity, k is the channel permeability, and ∇P is the fluid pressure gradient driving the flow. For parallel plate flow

$$k=h^2/12. \tag{2}$$

A fair amount of investigation has centered on developing a modification of Eq. (2) which would be predictive for flow in a real fracture; that is to say, one which accounts for the irregular surface profiles, alignment and partial contact of real fractures. Early measurements on smooth and rough noncontacting surfaces were reviewed by Witherspoon *et al.* [2] leading to the prediction

$$k=h^2/(12f), \tag{3}$$

where h is now to be interpreted as mean aperture width and the surface roughness factor f varied from 1.04 to 1.65. Previously, Lomize [3] had proposed the experimental form

$$f=1+6(\delta h/h)^{3/2}, \tag{4}$$

where δh is a measure of the surface roughness (asperite heights). Walsh and Brace [4] have proposed $f=T^2$, where T is a mean fracture tortuosity (ratio of actual to apparent path lengths). Notable work by Brown [5–7] provided a statistical quantification of fracture surfaces. More modern predictions, such as that by Zimmerman and Bodvarson [8],

$$k=\frac{h^2}{12}\left(1-\frac{3\sigma_h^2}{2h^2}\right)(1-2C), \tag{5}$$

incorporate higher-order statistical moment measures. Here σ_h is the standard deviation of the aperture width, and C is the fractional contact area between the two surfaces. Among other models, we mention that of Drazer and Koplik [9] that is based upon two-dimensional lattice Boltzmann simulations in channels between artificially generated rough surfaces having small height variation.

Our interest is in numerical computation of real fracture flow, specifically utilizing the lattice Boltzmann (LB) method to approximate Navier-Stokes flow. Among the earliest numerical computations of fracture flow were those by Brown and co-workers [6,10] using finite difference solutions to Reynolds equation. Ge [11] has recently introduced a general governing equation for fluid flow in a single fracture bounded by rough surfaces. The governing equation reduces to Reynolds equation if variations in tortuosity and aperture are small. Verberg and Ladd [12] have applied three-dimensional LB computations to a digitized geometry obtained by profiling real fractures. There however, the computed flow field was used primarily to compare the performance of the second-order continuous bounce back condition.

To our knowledge, no LB computations on fracture flow have been compared with permeability measurements from real data sets. Our purpose in this paper is to examine the performance of LB numerical simulation for permeability computation and to compare the results with experimental measurements taken on the same fracture samples upon

*Electronic address: ibkim@ams.sunysb.edu
†Electronic address: lindquis@ams.sunysb.edu
‡Electronic address: durham1@llnl.gov

which the digitized computations are based. Both laboratory and computational results were obtained at several values of mean aperture.

Our underlying physical interest is the behavior of rock fractures at midcrustal depths for which evidence [13] exists of fracture permeabilities several orders of magnitude higher than bulk permeability of most unfractured rock. Durham *et al.* [14,15] have profiled laboratory-produced fracture surfaces and conducted permeability studies [15] under various confining pressures (and hence mean apertures) appropriate to midcrustal depths. Two of these profiled data sets have been used in the numerical flow computations considered in this study.

The lattice Boltzmann method used in our computations is presented in Sec. II. Parallel plate validation studies are given in Sec. III. A description of the two data sets utilized in this study is presented in Sec. IV. Parallelization of the LB scheme is addressed in Sec. V. Results from the LB simulations and comparison with laboratory measurements are presented in Sec. VI. Discussion follows in Sec. VII.

II. THE FINITE DIFFERENCE LATTICE BOLTZMANN SCHEME

The LB method has been used as a numerical method for simulating Navier-Stokes flow since its introduction in 1988 [16]. Attractive features of the method include its handling of complicated geometries, appropriate for flow through porous media where wall boundaries are extremely irregular; the localization and ease of implementation of the computational scheme; and relative ease of parallelization, an added attraction for massive computations. On the negative side are the extreme numbers of iterations typically needed to compute steady state conditions; difficulties in implementing some types of boundary conditions; and the limited range of physical and chemical terms that can be modeled.

The LB method [16] is a finite difference method for solving the Boltzmann equation for a discrete velocity distribution,

$$\frac{\partial f_i}{\partial t}+\mathbf{e}_i\cdot\nabla f_i=\Omega_i+\frac{\mathbf{b}_f\cdot\mathbf{e}_i}{N_b c^2},\quad i=0,\ldots,N-1. \tag{6}$$

$f_i(\mathbf{x},t)$, $\mathbf{e}_i$, and $\Omega_i(\mathbf{x},t)$ are, respectively, the particle distribution function, the velocity, and the collision operator in the ith direction at each space-time point $\mathbf{x},t$. N is the number of discrete directions considered in the model. $\mathbf{b}_f(\mathbf{x},t)$ is an external body force vector that will be used to simulate a pressure gradient to drive fluid motion; c denotes particle speed; and N_b denotes the number of the discrete directions i that have nonzero projection onto $\mathbf{b}_f$. The LB method uses a Bhathagar, Gross, and Krook [17] relaxation term instead of a full nonlinear collision operator, specifically the single-time relaxation approximation, $\Omega_i=-(f_i-f_i^{\mathrm{eq}})/\tau$. Here $f_i^{\mathrm{eq}}(\mathbf{x},t)$ is the local equilibrium population distribution and τ is the relaxation time. The first several velocity moments of the equilibrium population distribution must match those of a Maxwellian distribution to ensure macroscopic Navier-Stokes behavior [18]. From the particle distribution functions and velocities, macroscopic values for density ρ and momentum are defined by

$$\rho=\sum_{i=0}^{N-1} f_i, \tag{7}$$

$$\rho\mathbf{u}=\sum_{i=0}^{N-1} f_i\mathbf{e}_i. \tag{8}$$

In three-dimensions, we utilize $N=27$ directions (the so-called 3D27Q model [19].) In this model the discrete velocities are

$$\mathbf{e}_i=\begin{cases} c(0,0,0), & i=0\\ c(\pm1,0,0), c(0,\pm1,0) & \\ c(0,0,\pm1), & i=1,\ldots,6\\ c(\pm1,\pm1,0), c(\pm1,0,\pm1) & \\ c(0,\pm1,\pm1), & i=7,\ldots,18\\ c(\pm1,\pm1,\pm1), & i=19,\ldots,26. \end{cases} \tag{9}$$

The equilibrium particle distribution function is

$$f_i^{\mathrm{eq}}=C_i\rho\left(1+\frac{3(\mathbf{e}_i\cdot\mathbf{u})}{c^2}+\frac{9(\mathbf{e}_i\cdot\mathbf{u})^2}{2c^4}-\frac{3\mathbf{u}\cdot\mathbf{u}}{2c^2}\right),\quad i=0,\ldots,26, \tag{10}$$

where

$$C_i=\begin{cases} 8/27, & i=0\\ 2/27, & i=1,\ldots,6\\ 1/54, & i=7,\ldots,18\\ 1/216, & i=19,\ldots,26. \end{cases} \tag{11}$$

Starting with a first order, upwind discretization of Eq. (6),

$$f(\mathbf{x}+\mathbf{e}_i\Delta t,t+\Delta t)=f(\mathbf{x},t)+\Omega_i+\mathbf{b}_f(\mathbf{x},t)\cdot\mathbf{e}_i/(N_b c^2),\quad i=0,\ldots,N-1, \tag{12}$$

a Chapman-Enskog expansion can be used [18] to show that the macroscopic behavior of this isothermal model produces the Navier-Stokes equations, plus terms of order M^2,

$$\partial_t\rho+\partial_\alpha\rho u_\alpha=O(M^2), \tag{13}$$

$$\rho\partial_t u_\alpha+\rho u_\beta\partial_\beta u_\alpha=-\partial_\alpha P+\partial_\beta(\mu(\partial_\beta u_\alpha+\partial_\alpha u_\beta))+b_f+O(M^2) \tag{14}$$

with viscosity μ, Mach number M, and Reynolds number R_e given by

$$\mu=(\tau-1/2)\rho c_s^2, \tag{15}$$

$$M=U/c_s, \tag{16}$$

$$R_e \equiv \frac{\rho UL}{\mu} = \frac{UL}{(\tau - 1/2)c_s^2}. \tag{17}$$

U and L are, respectively, a macroscopic speed and length scale characteristic of the flow. The sound speed for the model is $c_s = c/\sqrt{3}$.

Note that Eq. (12) restricts $\Delta x_\alpha = e_{i\alpha}\Delta t$, $\alpha = 1,2,3$, implying a uniform spatial grid spacing in all dimensions. For higher-order accuracy, and to enable different grid spacing in each dimension, we utilize a second-order finite difference lattice Boltzmann (FDLB) solver [20] in which central differencing is used for the spatial derivatives in the convective term,

$$\frac{\partial f}{\partial x_\alpha} \approx D_\alpha^c \equiv \frac{f(x_\alpha + \Delta x_\alpha, t) - f(x_\alpha - \Delta x_\alpha, t)}{2\Delta x_\alpha}, \quad \alpha = 1,2,3, \tag{18}$$

producing the spatial discretization

$$\frac{\partial f_i}{\partial t} = -\mathbf{e}_i \cdot (D_1^c f_i, D_2^c f_i, D_3^c f_i) - \frac{1}{\tau}(f_i - f_i^{\mathrm{eq}}) + \frac{\mathbf{b}_f \cdot \mathbf{e}_i}{N_b c^2}. \tag{19}$$

The time discretization is done via second-order Runge-Kutta

$$k_i^0 = \Delta t G_i(f_i(\mathbf{x}, t_n), t_n), \tag{20}$$

$$k_i^1 = \Delta t G_i(f_i(\mathbf{x}, t_n) + k_i^0, t_n + \Delta t), \tag{21}$$

$$f_i(\mathbf{x}, t_{n+1}) = f_i(\mathbf{x}, t_n) + \tfrac{1}{2}(k_i^0 + k_i^1), \tag{22}$$

where $G_i(f_i, t)$ denotes the right-hand side of Eq. (19). A Chapman-Enskog expansion for Eq. (22) replicates [19] the results of (13)–(17) with the replacement $(\tau - 1/2) \to \tau$.

Initial conditions on the f_i can be set by requiring $f_i(\mathbf{x},0) = f_i^{\mathrm{eq}}(\rho(\mathbf{x},0), u(\mathbf{x},0))$ using Eq. (10). With an initial velocity $u = 0$, Eq. (10) simplifies to partitioning the density amongst the N discrete directions at each point according to the weights C_i. Boundary conditions are generally more problematic since the fundamental quantities f_i in Eq. (6) are not the same as the macroscopic variables in which boundary conditions are usually formulated. Three boundary conditions concern us in our computations, the solid rock wall defining the upper and lower limits of the fracture (the z direction); the inlet-outlet boundary conditions in the flow direction (the x direction); and the flow seal restraining the fracture flow in the y direction.

Periodic boundary conditions are the easiest to implement in LB calculations. We, therefore, use periodic boundary conditions on the y direction endplanes of the fracture (perpendicular to the flow direction) to approximate the flow seal. The body force term, used to mimic a pressure gradient $\mathbf{b}_f = \nabla P$ driving the flow, obviates the need to explicitly set separate pressures at inlet and outlet. Thus periodic boundary conditions were also used for the inlet-outlet. Using periodic boundary conditions creates a problem when simulating real fractures, since geometries of the fracture at the two ends involved will not be in alignment. Our solution is to double the fracture in each periodic direction by attaching a mirror image of the fracture at one end. The new fracture is now twice the length, but with geometrically matching ends. Since we impose periodic boundary conditions in the x and y directions, this expands the computational volume by a factor of 4; clearly an expensive option in terms of memory and CPU time. We address this problem using parallel computation.

The implementation of no-slip wall-boundary conditions has been the subject of some discussion. The bounce-back scheme is one of the most popular implementations for complex wall geometries; when streaming to a wall node, the particle distribution scatters back to the node whence it came. Bounce back is locally first-order accuracy at boundaries [21]. A number of other schemes have been proposed [22–25]. We have found these schemes to be complicated to implement for irregularly shaped boundaries and have instead implemented the following scheme for updating wall boundary nodes and enforcing no slip.

(1) An intermediate solution $\hat{f}_i(\mathbf{x}_b, t + \Delta t)$ is generated at a wall boundary point $\mathbf{x}_b$ using Eqs. (20)–(22) with the exception that any second-order derivative D_c^α in $G_i(\cdots, \cdots)$ is replaced by a first-order upwind derivative

$$\frac{\partial f}{\partial x_\alpha} \approx D_\alpha^{\mathrm{up}} \equiv \frac{f(x_\alpha + \Delta^{\mathrm{up}} x_\alpha, t) - f(x_\alpha, t)}{\Delta^{\mathrm{up}} x_\alpha}, \quad \alpha = 1,2,3, \tag{23}$$

whenever a node internal to the wall would be required by the central difference formula (18). Nodes internal to the wall are, therefore, avoided in implementing spatial differencing.

(2) Final update values for each wall-boundary node are then computed as appropriate averages of $\hat{f}$ values

$$f_i(\mathbf{x}_b, t + \Delta t) = \hat{f}_{\bar{i}}(\mathbf{x}_b, t + \Delta t) = [\hat{f}_i(\mathbf{x}_b, t + \Delta t) + \hat{f}_{\bar{i}}(\mathbf{x}_b, t + \Delta t)]/2, \tag{24}$$

where $\bar{i}$ denotes the direction opposite to i. This ensures explicit enforcement of no-slip momentum conditions at wall-boundary nodes.

We have not ascertained the overall order of accuracy of this mixed first- and second-order no-slip boundary condition. Using the validation computations described in the following section, we have ascertained that the boundary conditions produce more accurate computation of flow field in the vicinity of the wall boundary than simple bounce back.

III. PARALLEL PLATE VALIDATION STUDIES

We have validated our FDLB solver on a slight variation of a standard problem; we consider steady state Poiseuille flow between parallel plates separated by distance L_z with the addition of a rectangular neck of width h placed in the flow path. The channel geometry is shown in Fig. 1. Flow is

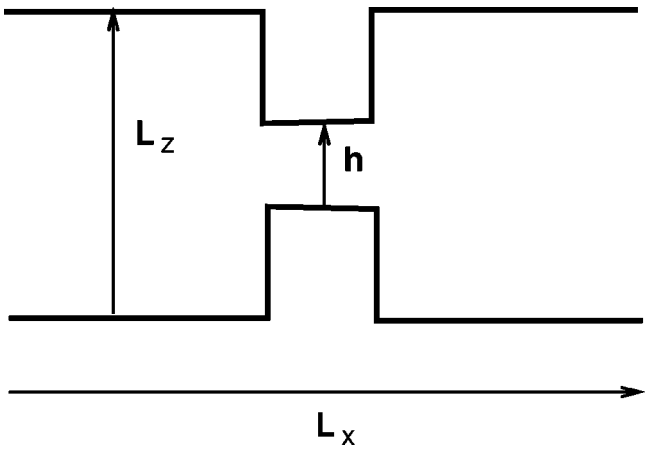

FIG. 1. The geometry of parallel plates, of separation L_z, with a rectangular constrictive slot of separation h.

induced by a constant body force in the x direction; periodic boundary conditions are used for the inlet-outlet and y directions; the wall boundary condition is used at the plate surfaces.

The analytic solution $(u_x(z),0,0)$ for the velocity is known for the case $h=L_z$,

$$u_x(z)=u_{max}4\frac{z}{L_z}\left(1-\frac{z}{L_z}\right), \quad z\in[0,L_z], \tag{25}$$

where $u_{max}=L_z^2|\nabla P|/(8\mu)$.

Figure 2 compares the prediction of Eq. (25) with the computational result for $u_x(x=5,y=5,z)$, for a fluid having $c=1$ mm/sec and density $\rho=10^{-3}$ gm/mm^3 driven by a pressure gradient $|\nabla P|=10^{-6}$ gm/mm sec^2. Two fine grid computations are shown, for $R_e=0.1$ and $R_e=1$. (The computational result is virtually independent of the x,y coordinate of the point of comparison.)

The computation was declared to have reached steady state when the relative change in the L_2 norm of the time step velocity difference was less than input tolerance,

$$\frac{\sqrt{\sum_{\mathbf{x}}|\mathbf{u}(\mathbf{x},t+\Delta t)-\mathbf{u}(\mathbf{x},t)|^2}}{\sqrt{\sum_{\mathbf{x}}|\mathbf{u}(\mathbf{x},t)|^2}}\leqslant \text{tol}. \tag{26}$$

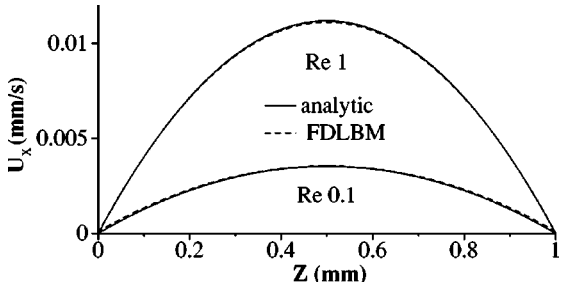

FIG. 2. Comparison of analytic and FDLB computation for the steady state Poiseuille flow between parallel plates. The computational geometry is $L_x=L_y=10$ mm, and $L_z=1$ mm; the grid spacings are $\Delta_x=\Delta_y=1$ mm and $\Delta_z=0.01$ mm.

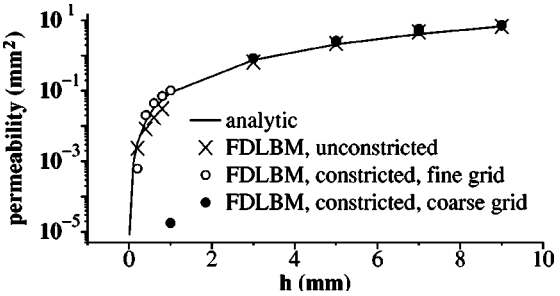

FIG. 3. Permeability vs the smallest channel width between parallel plates. The solid curve represents the analytical, parallel plate solution, with separation h. x represents computed results for parallel plates of separation h (no flow constriction). Circular points represent computed results for parallel plate of separation L_z with a restricted neck of width $h<L_z$.

These validation computations were done in double precision; the value of tol was set to 10^{-8}.

Comparisons between computed and analytic predictions of parallel plate permeability are shown in Fig. 3. The solid line is the analytic prediction (2) and points marked "x" are computed results. Here the computational domain is $L_x=L_y=10$, and $L_z=h$ is variable; $\rho=10^{-3}$ gm/mm^3, $\tau=1$ sec, $c=1$ mm/sec, and $|\nabla P|=10^{-5}$ gm/mm sec^2. The agreement is excellent, given the coarseness of the grid, $\Delta x=\Delta y=1$, $\Delta z=0.2$.

We now consider parallel plate flow through a constrictive neck $h<L_z$. Intuitively, for incompressible flow, the permeability should be dominated completely by the neck width h. This is confirmed in Fig. 3 that also plots (open and filled circles) permeabilities computed for flows through constrictive necks of variable widths h. The permeability through the constrictive parallel plate geometry is determined solely by the neck width h, the resultant permeability is that equivalent to flow through an unconstricted parallel plate of width $h=L_z$.

An interesting steady state solution is obtained when the constriction is completely closed off. Computed velocity and density fields are shown in Fig. 4 for the cases $h=L_z$, $h=L_z/3$, and $h=0$. If there is no constriction ($h=L_z$), the steady state density is constant, and the flow modeled is effectively incompressible. However, in the presence of flow constrictions ($h=L_z/3$), density gradients appear. These density gradients arise in direct response to the body force used to drive the flow.

In the case in which the constriction is total, rather than zero flow (which would be expected when attempting to drive incompressible fluid under pressure gradient into a closed fracture) the numerical solution shows two counter-rotating vortices. The rotating vortices set up a net x component of flux as summarized in the last row of Table I. In the case of complete flow constriction, the density gradients are achieved through the establishment of counter-rotating vortices. The presence of the density gradient is presumably due to the $O(M^2)$ compressibility error terms in Eqs. (13) and (14) by which the LB method deviates from incompressible Navier-Stokes flow. As long as the constrictive channel is open, the $O(M^2)$ terms remain "small." When through flow

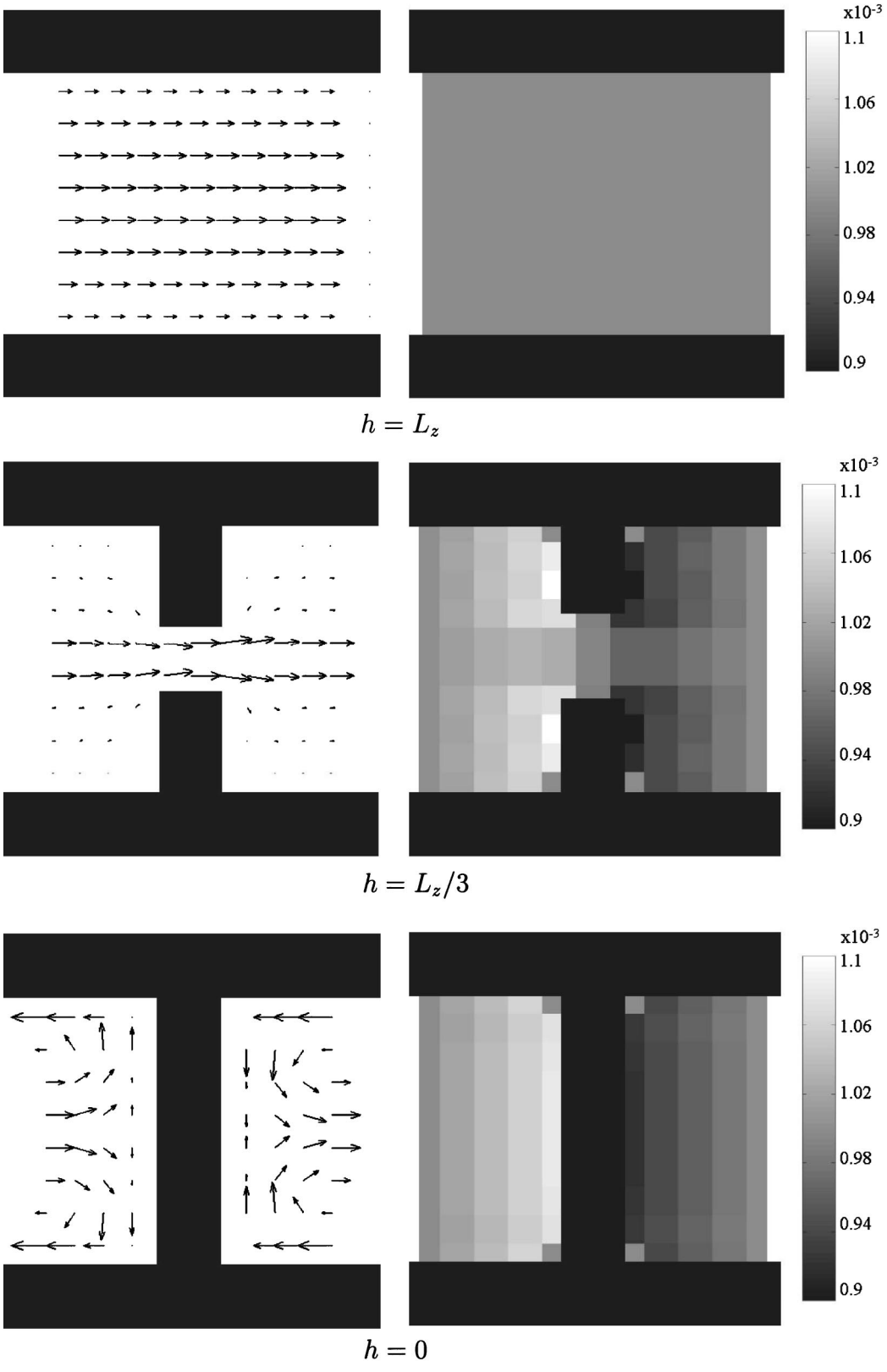

FIG. 4. Mid-fracture transects of the (left) velocity field projected onto the xz plane and (right) density (gm/mm^3) for steady state flow though constrictive neck geometry of Fig. 1. The domain considered is $10\times10\times9$ mm^3. The illustrated computations are on a coarse grid $\Delta x=\Delta y=\Delta z=1$ mm.

TABLE I. Total flux (mm^3/sec) through the constrictive plate cross section as a function of distance x along the flow direction. Numbers in brackets indicate power of ten.

h	x (mm)						
(mm)	0	2	4	5	6	8	10
9	9.896	9.896	9.896	9.896	9.896	9.896	9.896
3	1.146	1.097	1.106	1.161	1.222	1.201	1.146
0	2.4[−5]	1.48[−4]	0.0	0.0	0.0	2.37[−4]	2.4[−5]

is impossible, the $O(M^2)$ terms become dominant and drive the flow into a solution regime incorrect for incompressible flow.

IV. PROFILED HARCOURT GRANITE FRACTURES

Laboratory measured geometrical and permeability data were obtained for a fracture in Harcourt granite (HG), a medium to coarse grained granite from South Australia. A single tensile fracture was produced using the so-called ''Brazilian'' technique [26]. The sample consisted of a cylindrical core fractured along its axis (x direction). The core was approximately 140 mm in diameter and 164 mm in length. We designate the x direction to be along the core axis, and the z direction to be ''perpendicular'' to the fracture surfaces. A 116×128 mm^2 area of the fracture was profiled at 1 mm spacing in both horizontal (x,y) directions [27]. Both upper and lower faces of the fracture were profiled with horizontal registration between corresponding points on the two surfaces good to within 0.05 mm. Profile measurements (z direction) are accurate to within 8 μm. We refer to this data set as the mated configuration, HG3.

A second set of geometrical and permeability data were measured on the same rock, but with the two rock halves shifted with respect to one another by 0.5 mm in the x (flow) direction. We refer to this as the offset configuration HG3F. Note that the offset was achieved not by sliding, but by separating the mated rock halves, displacing one of them 0.5 mm in the axial direction, and then placing them back together. The profiles in the offset configuration were 111×128 mm^2, profiled again at 1 mm spacing.

Consider an arbitrary reference plane $z=0$. The upper $(+)$ and lower $(-)$ surfaces of the fracture are described by

$$z^+(x,y)=h_0^+-h^+(x,y),$$
$$z^-(x,y)=h_0^-+h^-(x,y). \tag{27}$$

Here h_0^+ and h_0^- are z values relative to which h^+ and h^- are measured. The subtraction and addition asymmetries in the definitions of z^+ and z^- arise from a difference in sign convention for h^+ and h^-. *h^+ is defined to be positive in the downward direction*; *h^- is defined to be positive in the upward direction*. This convention derives from the laboratory profilometry used to measure h^+ and h^-. In profilometry, the two rock halves are laid open, side by side, fracture surface upward, and profiles are taken on both halves. *In this profilometry configuration, h^+ and h^- are defined with consistent signs*. The fracture aperture is

$$\begin{aligned} a(x,y;A)&\equiv z^+(x,y)-z^-(x,y),\\ &=(h_0^+-h_0^-)-(h^++h^-),\\ &\equiv A-z(x,y), \end{aligned} \tag{28}$$

where the definitions of A and z are clear from context.

Profilometry directly measures $h^-(x,y)$ and $h^+(x,y)$, or equivalently, their sum $z(x,y)$. Determination of the constant A needed to obtain the true, unconfined, fracture aperture $a(\cdots)$ requires careful experimental registration of the two halves of the fracture when they are separated for profilometry, accurate measurements of the increased diameter induced in the core after fracturing due to relaxation of stresses and to near-surface inelastic deformation associated with fracturing, and estimation procedures to account for gaps induced by small amounts of loose shattered material. Such accounting for the profiled configuration HG3 indicates a value of $A=0.19\pm0.03$ mm.

We are interested in computationally varying the aperture. From Eq. (28) we can define a variable mathematical aperture

$$a(x,y;A,t)\equiv A-t-z(x,y). \tag{29}$$

The ''push-down'' t is an arbitrary parameter by which we can artificially widen or contract the aperture of the fracture. (It mimics the variable confining pressure used in laboratory experiments to change the aperture width.) Note that as t increases from zero, sections of the lower and upper surfaces begin to overlap, simulating contact. The overlap is unphysical; in real rock, under increasing confining pressure, areas of contact between the two surfaces will locally deform in a complex manner. *We ignore the presence of such deformation in our study*. To compensate for overlapping portions of the surfaces under change in A, we redefine the variable aperture a as

$$a(x,y;A,t)\equiv\begin{cases} A-t-z(x,y) & \text{if } A-t-z(x,y)>0\\ 0 & \text{otherwise.}\end{cases} \tag{30}$$

From now on we shall refer to $a(x,y;A,t)$ simply as the aperture of our model fracture. We denote the mean aperture of $a(\cdots)$ as $a_m\equiv\langle a(x,y;A,t)\rangle$, where the average is over all profiling locations x,y. We define the fractional contact area C between the upper and lower surfaces of our model fracture as the fraction of sites x,y for which $a(x,y;A,t)=0$ in Eq. (30). For brevity, we shall refer to C as the contact area.

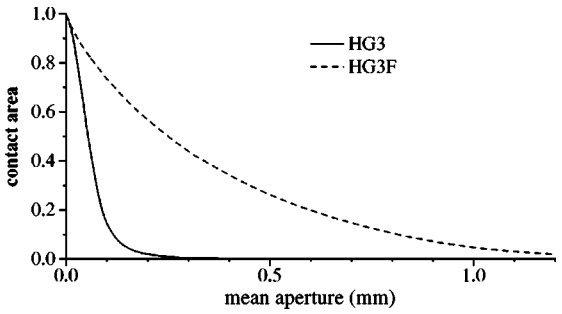

FIG. 5. Contact area C as a function of mean aperture for the two profiled configurations HG3 (mated) and HG3F (offset).

Figure 5 plots the contact area C between the two surfaces as a function of mean aperture a_m for both mated and offset configurations. It is important to note that the $C(a_m)$ relationship in Fig. 5 *is independent of choice of A.* (If A is changed, then the push-down t required to achieve a specific value of a_m will also change, resulting in the same a_m, C point in Fig. 5.) The $C(a_m)$ relationship is solely a property of the measured profile $z(x,y)$.

Our interest is in computing permeability as a function of mean aperture and comparing with laboratory measurements. Consequently it is useful to know at what contact area, complete loss of flow in the fracture can be expected. (This is referred to as the percolation threshold of the fracture.)

The percolation threshold was estimated using medial axis analysis [28,29]. Briefly, for each value of C, the medial axis transform was used to trace all possible paths through the aperture connecting ''inlet'' to ''outlet.'' If any inlet-to-outlet connection existed, the fracture was deemed capable of supporting flow. Using a bisection search on C, bounding values on the percolation threshold contact area for flows separately in the x and y directions were obtained as shown in Table II.

Permeabilities were experimentally measured for HG3 and HG3F under steady state flow conditions using tap water as a fluid. All measurements were made at room temperature. The outlet pressure was fixed at 0.1 MPa (1 atm). For the mated fracture, HG3, confining pressures varied from 0.21 MPa to 80 MPa, and pressure differences driving the flow varied from 5 KPa at the lowest confining pressure, to 10 MPa at the highest. For the offset fracture HG3F confining pressures varied from 0.1 MPa to 160 MPa, and pressure differences driving the flow varied from 120 Pa at the lowest confining pressure to 4.4 KPa at the highest. Permeability was determined from Eq. (1) using the cross sectional area of the cylindrical core face at the outlet. The laboratory permeability measurements on a fracture were performed as a sequence of measurements with confining pressure *increasing* for each new data point. Plastic strain and structural damage preclude lowering confining pressure to check reproducibility. Typically each permeability measurement involved measuring the time to flow 25 mL of water through the fracture.

TABLE II. Bounding intervals determined for percolation threshold values C_x and C_y of contact area in x and y directions, respectively.

	C_x	C_y
HG3	(0.441,0.467)	(0.623,0.646)
HG3F	(0.560,0.588)	(0.430,0.463)

V. PARALLELIZATION

With the data profiled at 1 mm spacing in the x and y directions, interpolation must be used if a finer numerical horizontal grid spacing is desired. We avoid interpolation and use $\Delta x = \Delta y = 1.0$ mm. In the case of the mated configuration HG3, when the contact area $C=0$, the maximum value of the aperture profile is $\max_{x,y} z(x,y) = 12.09$ mm and the mean aperture is 0.94 mm. At a near-percolation threshold value of $C=0.5$, while the mean aperture of 0.09 mm is now much smaller, $z_{max} = 11.29$ mm is still large. Thus with a grid spacing of $\Delta z = 0.05$ mm, the numerical grid size will require $11\times10^6 - 14\times10^6$ nodes. (Recall the doubling of the fracture in the x and y directions to implement periodic boundary conditions.) As a compromise between memory requirement, CPU time, and communication cost, we store four single precision floats $f_i^{\mathrm{eq}}(\cdots,t_n)$, $f_i(\cdots,t_n)$, $f_i(\cdots,t_n+\Delta t)$ from Eq. (21), and $f_i(\cdots,t_{n+1})$ for each link of each node. For 3D27Q, we, therefore, store 432 bytes of information per node. Thus a naive computation gives memory requirements of 6 Gbytes for a computation on a $232\times256\times243$ node grid. A major savings in memory is accomplished by assigning no storage to any node lying outside of the open aperture region (with an exception for wall boundary nodes). Depending on the contact area, this reduces memory requirements to $2-16\,\%$ of the naive value. Even with this reduction, parallel implementation is required. Parallelization was done using nonoverlapping, ''bread slice,'' domain decomposition in the flow direction. Load balancing was achieved by adjusting the widths of individual domain slices so that the each contained approximately the same number of aperture nodes. Message passing was done with the MPI interface. Computations were performed on the Stony Brook Galaxy, a Beowolf class cluster having 256 Pentium processors, each processor having 512 Mbytes of RAM. Parallel performance of the FDLB implementation is discussed in Ref. [29]. Typically, a simulation required nearly 340 h using 8 Pentium II processors to achieve steady state [as determined by Eq. (26) with a tolerance tol $=10^{-5}$] in $\approx10^5$ iterations.

VI. NUMERICAL RESULTS

In parallel with the laboratory permeability measurements performed on HG3 and HG3F, we numerically compute the steady state flow of water ($\mu = 0.001$ Pa sec, $\rho = 0.001$ gm/mm^3) through the fracture. The particle speed c required in the LB formulation was chosen as a multiple of the average velocity of the water measured in the corresponding experiment. Mach numbers varied but were in the range from 10^{-2} to 10^{-1}. While pressure gradients were not available for all experimental measurements, pressure drops across the cylinder core were measured for the lowest and

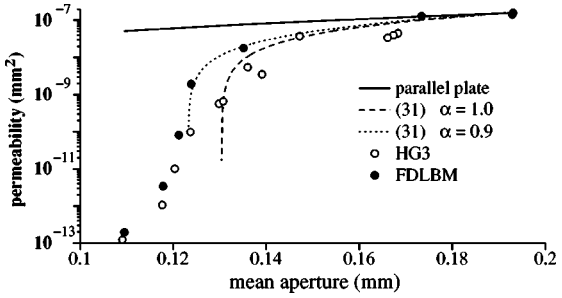

FIG. 6. Comparison between computed (FDLBM), experimental (HG3), parallel plate model, and Eq. (31) values of permeability versus mean aperture for the mated Harcourt granite fracture.

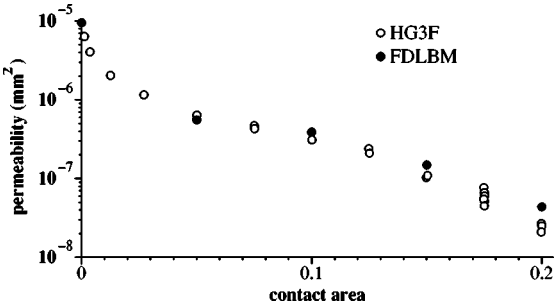

FIG. 7. Comparison between computed (FDLBM) and experimental (HG3F) values of permeability versus contact area C for the offset Harcourt granite fracture.

highest confining pressure runs. Pressure gradients for intermediate confining pressures were approximated using linear interpolation.

Figure 6 summarizes the comparison between the computed and measured values of permeability versus mean aperture for the mated fracture HG3. The mean aperture values for the laboratory measurements are mechanical mean apertures, computed from fracture closure measurements. The laboratory permeability measurements were normalized by the cross sectional area of the cylindrical core. Since the entire cross sectional area was not modeled numerically, the numerical permeabilities were normalized to agree with the laboratory measurements at the highest mean aperture setting (lowest confining pressure on the fracture). The numerical permeabilities tend to exceed the experimental permeabilities (worst case is a factor of 10) but capture the experimental permeability trend very well.

The prediction of the parallel plate model, based upon $h = a_m$, also shown in Fig. 6 does very poorly in capturing the trend. So will Eq. (3) for any constant value of f. This is hardly unexpected, our simple constricted-neck parallel plate model would lead us to conclude that a_m is a poor indicator of the constrictive fracture width value that is effectively controlling the flow rate.

There is a problem in applying the Zimmerman-Bodvarson (ZB) prediction (5) to our fracture—the standard deviation of the fracture aperture is 70% of the true, unconfined, mean aperture and becomes larger than the mean aperture at 7% contact area ($a_m = 0.13$). Thus any factor of the form $1-\alpha(\sigma_h/h)^2$ as used in Eq. (5) is going to have a sharp ''knee'' behavior and very rapidly become negative at some mean aperture value. This is demonstrated in Fig. 6 using a generalized ZB prediction

$$k = \frac{h^2}{12}\left(1-\alpha\frac{\sigma_h^2}{h^2}\right)(1-2C), \tag{31}$$

for parameter values $\alpha = 0.9, 1.0$. We also note that the contact area factor $(1-2C)$ plays little role in the accuracy of the fit (31) to the experimental data.

For the offset data, HG3F, we have been unable to reconcile the mechanical mean apertures measured during the laboratory experiments with the mathematical mean apertures computed from the profiled data. Offsetting the top and bottom surfaces of the fracture may require a recalibration of the constant A in Eq. (28). As mean aperture is a very sensitive variable (i.e., small errors result in comparatively large changes in k), we, therefore, compare measured and computed permeabilities for the offset fracture as a function of a more robust variable, the contact area C. To estimate contact areas for the offset configuration, we note that measurements on a similar tensile-induced, offset fracture in Westerly granite [14] found surface contact ratios of approximately 20% at confining pressures of 160 MPa. *We therefore assume that the laboratory range of measured mean apertures for HG3F correspond to surface contact ratios in the range 0 to 20% and presume a linear relationship between confining pressure and surface area contact for the laboratory measurements.* (This assumption is also in accord with the mated data HG3. From Fig. 6 note that mean apertures vary from 0.2 down to 0.1, which, from Fig. 5, correspond to contact areas from 0 to 10%. As the mated configuration was subjected to a maximum confining pressure of only 80 MPa, this is consistent with our contact area assumption for the offset configuration.)

Figure 7 compares measured and computed permeabilities for the offset fracture as a function of contact area. Numerical computations were performed at $C = 0$, 0.05, 0.1, 0.15, and 0.2 and compare surprisingly well with the laboratory measurements. Note repeated laboratory permeability measurements at several values of C. For these measurements, the confining pressure was held constant and several permeability measurements taken over a period of time. The largest set of measurements were taken at a confining pressure of 140 MPa (contact area of 0.175), where five permeability measurements were taken over a 5 h period. A slow decrease in permeability with time is observed in all such repeated measurements for this fracture. We postulate that the time dependent decrease in permeability is due to increased clogging resulting from the movement of fines, the clogging occurring either in the fracture or in the fluid collection tubing at the outlet. We further note that the set of permeability measurements taken at $C = 0.2$ were performed a day later than the others; the confining pressure was removed overnight and then reapplied the next day.

VII. DISCUSSION

There are clearly several factors that affect the agreement between the numerical and experimental results.

One factor is the discretization of the fracture surface. With profiling locations spaced at 1 mm, we are resolving the surface feature only above wavelengths of 1 mm; the effect on flow for features below 1 mm wavelength is of unknown magnitude. A second feature of discretization is the ''Manhattan'' skyline nature of a discretized surface, which makes computation of surface-surface contact area easier, but simplifies the true ''mountain'' topography of a fracture surface.

Ignoring stresses induced in the surfaces when numerically pushing the fracture surfaces together is a second factor. The elastic and plastic changes so induced in the surface profiles of a real fracture were not captured in the numerical aperture. The numerical ''push-through'' of the fracture surfaces also produces missing mass that remains unaccounted for.

The absence of recorded values for fluid pressure gradients for some of the experimental measurements, and the decision to use contact area as the comparing parameter for the offset data, lead to the use of linear interpolation to provide necessary numerical parameters. The error introduced in using the interpolated values is unknown.

The use of laboratory measured average water velocity values for the particle speeds required in the LB calculations undoubtedly works in a manner to improve the accuracy of the calculations.

From the constrictive plate studies, we note that the presence of the compressible $O(M^2)$ terms in the LB method will cause density variations in the rough geometry aperture. The overall effect of these variations on the resultant flow is unknown.

While the LB implementation used here gives reasonably good permeability predictions, the computational cycles required to compute steady state flow are very large. Several steps can be implemented to improve the computational time. Use of the 15-velocity, 3D15Q, [25] should improve the speed (and memory) by a factor of almost 2 without accuracy loss. Use of direct inlet-outlet pressure conditions [25] rather than imposing a body force to drive the flow would obviate the need to double the domain in the flow direction, again at a factor of two savings in speed and memory. The time independent LB method developed in Ref. [30] would be expected to improve the computational performance by a factor of 1–2 orders of magnitude, depending on mean aperture. It would be interesting to investigate all of these three improvements in the context of the nonconstant grid spacing finite difference method.

ACKNOWLEDGMENTS

This work was supported by the Geosciences Program of the U.S. Department of Energy, Grant No. DE-FG02-92ER14261 (I.K. and W.B.L.); the Applied Mathematics Subprogram of the U.S. Department of Energy, Grant No. DE-FG02-90ER25084 (W.B.L.); and the U.S. Department of Energy under Contract No. W-7405-ENG-48 to Lawrence Livermore National Laboratory (W.B.D.).

[1] R.L. Kranz, A.D. Frankel, T. Engelder, and C.H. Scholz, Int. J. Rock Mech. Min. Sci. Geomech. Abstr. **16**, 225 (1979).
[2] P.A. Witherspoon, J.S.Y. Wang, K. Iwai, and J.E. Gale, Water Resour. Res. **16**, 1016 (1980).
[3] G.M. Lomize, *Flow in Fractured Rocks* (Gosenergoizdat, Moscow, 1951).
[4] J.B. Walsh and B.F. Brace, J. Geophys. Res. B **89**, 9425 (1984).
[5] S.R. Brown and C.H. Scholz, J. Geophys. Res. **90**, 5531 (1985).
[6] S.R. Brown, J. Geophys. Res. **92**, 1337 (1987).
[7] S.R. Brown, J. Geophys. Res. **94**, 9429 (1989).
[8] R.W. Zimmermann and G.S. Bodvarson, Transp. Porous Media **23**, 1 (1996).
[9] G. Drazer and J. Koplik, Phys. Rev. E **62**, 8076 (2000).
[10] S.R. Brown, H.W. Stockman, and S.J. Reeves, Geophys. Res. Lett. **22**, 2537 (1995).
[11] S. Ge, Water Resour. Res. **33**, 53 (1997).
[12] R. Verberg and A.J.C. Ladd, Phys. Rev. Lett. **84**, 2148 (2000).
[13] W.F. Brace, Int. J. Rock Mech. Min. Sci. Geomech. Abstr. **17**, 241 (1980).
[14] W.B. Durham and B.P. Bonner, J. Geophys. Res. **99**, 9391 (1994).
[15] W.B. Durham, J. Geophys. Res. **102**, 18 405 (1997).
[16] G. McNamara and G. Zanetti, Phys. Rev. Lett. **61**, 2332 (1988).
[17] P.L. Bhathagar, E.P. Gross, and M. Krook, Phys. Rev. **94**, 511 (1954).
[18] J. Sterling and S. Chen, J. Comput. Phys. **123**, 196 (1996).
[19] X. He and L.S. Luo, Phys. Rev. E **56**, 6811 (1997).
[20] N. Cao, S. Chen, S. Jin, and D. Martinez, Phys. Rev. E **55**, R21 (1997).
[21] I. Ginzbourg and P.M. Adler, J. Phys. II **4**, 191 (1994).
[22] P.A. Skordos, Phys. Rev. E **48**, 4823 (1993).
[23] D.R. Noble, S. Chen, J.G. Georgiadis, and R.O. Buckius, Phys. Fluids **7**, 203 (1995).
[24] S. Chen, D. Martinez, and R. Mei, Phys. Fluids **8**, 2527 (1996).
[25] Q. Zou and X. He, Phys. Fluids **9**, 1591 (1997).
[26] J.C. Jaeger and N.G.W. Cook, *Fundamentals of Rock Mechanics* (Chapman and Hall, London, 1976).
[27] W.B. Durham and B.P. Bonner, Int. J. Rock Mech. Min. Sci. Geomech. Abstr. **30**, 699 (1993).
[28] W.B. Lindquist, A. Venkatarangan, J. Dunsmuir, and T.F. Wong, J. Geophys. Res. B **105**, 21509 (2000).
[29] I. Kim, Ph.D. thesis, Stony Brook University (2002).
[30] R. Verberg and A.J.C. Ladd, Phys. Rev. E **60**, 3366 (1999).